Identification of kite aerodynamic characteristics using the estimation before modeling technique

Borobia-Moreno, R.; Ramiro-Rebollo, D.; Schmehl, R.; Sánchez-Arriaga, G.

DOI
10.1002/we.2591

Publication date
2021

Document Version
Final published version

Published in
Wind Energy

Citation (APA)
Borobia-Moreno, R., Ramiro-Rebollo, D., Schmehl, R., & Sánchez-Arriaga, G. (2021). Identification of kite aerodynamic characteristics using the estimation before modeling technique. *Wind Energy*, *24*(6), 596-608. https://doi.org/10.1002/we.2591

Received: 8 March 2020 | Revised: 30 September 2020 | Accepted: 21 October 2020

DOI: 10.1002/we.2591

WILEY

RESEARCH ARTICLE

Identification of kite aerodynamic characteristics using the estimation before modeling technique

R. Borobia-Moreno[1,2] | D. Ramiro-Rebollo[2] | R. Schmehl[3] | G. Sánchez-Arriaga[2]

[1]Centro de Experimentación de "El Arenosillo" (CEDEA), Instituto Nacional de Técnica Aerospacial (INTA), Mazagón, Huelva, Spain

[2]Bioengineering and Aerospace Engineering Department, Universidad Carlos III de Madrid, Leganes-Madrid, Spain

[3]Faculty of Aerospace Engineering, Delft University of Technology, Delft, The Netherlands

Correspondence
G. Sánchez-Arriaga, Avenida de la Universidad 30, 28911, Leganes, Spain.
Email: gonzalo.sanchez@uc3m.es

Funding information
European Regional Development Fund, Grant/Award Number: ENE2015-69937-R; Ministerio de Ciencia e Innovación; Ministerio de Economía, Industria y Competitividad, Gobierno de España, Grant/Award Number: RYC-2014-15357; Agencia Estatal de Investigación of Spain, Grant/Award Number: PID2019-110146RB-I00

Abstract

The aerodynamic characteristics of a leading edge inflatable (LEI) kite and a rigid-framed delta (RFD) kite were investigated. Flight data were recorded by using an experimental setup that includes an inertial measurement unit, a GPS, a magnetometer, and a multi-hole Pitot tube onboard the kites, load cells at every tether, and a wind station that measures the velocity and heading angle of the wind. These data were used to feed a flight path reconstruction algorithm that estimated the full state vector of the kite. Since the latter includes the aerodynamic force and moment about the center of mass of the kite, quantitative information about the aerodynamic characteristics of the kites was obtained. Due to limitation of the experimental setup, the LEI kite flew most of the time in post-stall conditions, which resulted in a poor maneuverability and data acquisition. This assumption was corroborated by a particular maneuver where the lift coefficient decreased from 1 to 0.4, while its angle of attack increased from 35° to 50°. On the contrary, abundant flight data were obtained for the RFD kite during more than 10 figure-eight maneuvers. Although the angle of attack was high, between 20° and 40°, the kite did not reach its maximum lift coefficient. High tether tensions and a good maneuverability were achieved. Statistical analysis of the behavior of the lift, drag, and pitch moment coefficients as a function of the angle of attack and the sideslip angle allowed to identify some basic aerodynamic parameters of the kite.

KEYWORDS
aerodynamics, airborne wind energy, kite

1 | INTRODUCTION

The aerodynamics of small and micro aerial vehicles is currently an active field of research.[1,2] Besides the large number of applications, such as military, environmental monitoring, and the understanding of the flight of insects and small birds, the topic is scientifically relevant due to the coexistence of several interesting phenomena. These vehicles typically share a common set of characteristics that include low velocities, high angle of attack (often at post-stall), low aspect-ratio, Reynolds number of operation in the range from 10^2 to 10^5, and light and flexible structures. They also take advantage of non-stationary effects to reach better performance than conventional wings. An example is the dynamic stall, that is, the delay of conventional flow separation from wings due to an unsteady motion.[3,4]

Airborne wind energy (AWE) systems,[5] which are aircraft like rigid wings and flexible kites linked to the Earth by tethers, share some of the characteristics mentioned above and are excellent candidates to study and understand basic aerodynamic phenomena. Analysis of power generation in wind farms indicates that these systems can be economically attractive.[6] Whether the AWE system generates energy on the ground by using the tether tension or on board with wind turbines, the machine typically operates in cross-wind conditions. Circles and figure-eight trajectories yielding non-stationary aerodynamic conditions are typically implemented. Reaching high lift coefficients is important to maximize the performance. High-fidelity models and flight simulators[7-12] also play an important role during the design and optimization phases of the machines. Pioneering aerodynamic models[13-15] have been followed by studies with viscous-inviscid interaction methods,[16] Reynolds averaged Navier–Stokes simulations,[17,18] and large eddy simulations.[19] Most of the studies were dedicated to the analysis of leading edge inflatable and ram-air kites at stationary flow conditions.

Experimental studies on the aerodynamics of AWE systems were also carried out. Besides wind tunnel experiments,[13,19] flight test setups have been developed to determine the aerodynamic characteristics of AWE systems.[20-23] In situ flow measurements of a soft kite in complex flight maneuvers were obtained.[18,22] The Pitot tube was installed on a rigid frame attached to the two power lines, instead of the kite, and the inflow angles were measured with vanes. Other experimental setups did not include sensors for the in situ measurement of the aerodynamic velocity vector of the kite.[20,21,23] Even without such important information, the sensor data, for example, position and velocity of the kite, velocity and heading angle of the wind, and tether tensions, were used as inputs of extended Kalman filters (EKF),[20,23] which provided an estimation of the time history of the full state vector. Since the latter can include the aerodynamic force and torque about the center of mass, these setups are key elements to determine the aerodynamic model of kites by implementing the so-called estimation before modeling method.[24,25] Similar sensor fusion techniques have also been applied to provide kite position and heading feedback to autonomous kite control systems. Onboard measurements with inertial sensors have been combined with on ground measurements of the tether angles, radio range, or visual tracking using extended Kalman filters.[26,27]

This work presents flight data of two types of traction kites used for AWE systems. It demonstrates that, in the experimental setup, the kites fly at high angle of attack. Unlike previous work, the kites were equipped with a multi hole Pitot tube that took in situ measurements of the airspeed, the angle of attack and the sideslip angle. Such high-precision sensor, which was not used in past works on AWE systems due to its vulnerability and cost,[28] is of great importance for improving the estimation accuracy of the air flow parameters, and consequently for the aerodynamic characterization of the kite. Section 2 explains the main modifications with respect to a precursor study[20] that have been implemented in the experimental setup and the EKF. Sections 3 and 4 present the results obtained for a leading edge inflatable kite (LEI) and a rigid-framed (RFD) kite, respectively. Due to limitations of the experimental setup, the LEI kite flew in post-stall conditions and a disparate quantity of the flight data was obtained for the kites. For this reason, a deeper analysis of the aerodynamic characteristics of the RFD kite was carried out. The conclusions are summarized in Section 5.

2 | EXPERIMENTAL SETUP AND FLIGHT PATH RECONSTRUCTION ALGORITHM

A low-cost and portable experimental setup aimed at the flight testing of LEI kites was presented in a past work.[20] Its sensors provide the required information to feed a flight path reconstruction (FPR) algorithm that gives an off-line estimation of the trajectory in the state-space, that is, the evolution of the state vector during flight. This section is focussed on the main modifications that have been implemented in the experimental setup and the FPR algorithm to improve the estimation of the aerodynamic force and torque. Details can be found in that work and in Appendix A. We will use an Earth-fixed reference frame (S_E) with origin at the anchoring point of the kite with the ground (O_E), the x_{NED}-axis and the y_{NED}-axis pointing to the local geographic north and east, respectively, and z_{NED} completing a right-handed coordinate system, pointing downwards (Figure 1). Unit vectors along the axes of a given frame are $\boldsymbol{i}$, $\boldsymbol{j}$, and $\boldsymbol{k}$. Magnitudes measured by the sensors and variables of the observation vector of the EKF are denoted with a tilde on the top of a letter.

2.1 | Experimental setup

In addition to LEI kites, the experimental setup has been updated to test RFD kites (see top and bottom panels in Figure 2). The LEI kite used in the experiment is a Cabrinha Swichblade kite with five struts, and the RFD kite is an HQ Fazer XXL kite. For each of these, we introduce a frame of reference S_K with origin at the center of mass of the kite (O_K), and axes x_K and z_K spanning the plane of symmetry of the kite. The y_K-axis completes the right-handed frame. For the LEI kite (top panel), the x_K-axis is along the direction defined by the imaginary line that connects the leading and trailing edge and, for the RFD kite, the x_K-axis is along the longitudinal spine of the kite (bottom panel). The LEI kite has two rear lines and two front lines. The attachment points at the leading and trailing edges of the kite are denoted by $A^{\pm}$ and $B^{\pm}$, respectively, and their position vectors in the S_K-frame are $\overline{O_K A}^{\pm} = X_A \boldsymbol{i}_B \pm Y_A \boldsymbol{j}_B + Z_A \boldsymbol{k}_B$ and $\overline{O_K B}^{\pm} = X_B \boldsymbol{i}_B \pm Y_B \boldsymbol{j}_B + Z_B \boldsymbol{k}_B$. The RFD kite has two lines, and their attachment points at the kite are called $A^{\pm}$.

FIGURE 1 Experimental setup reference frames

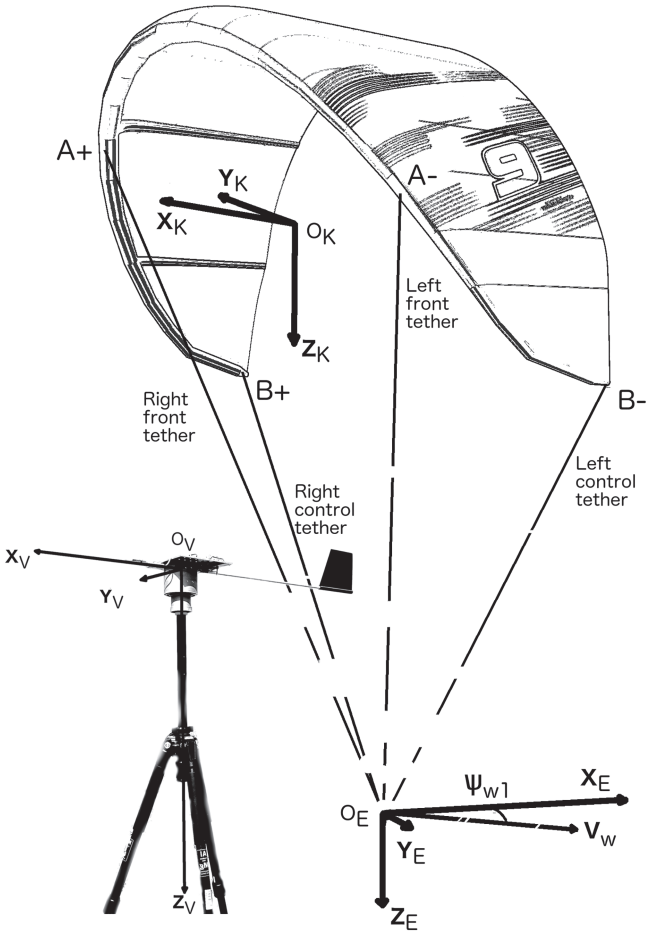

The kites are equipped with onboard sensors that provide measurements of the S_E-components of the position ($\tilde{\boldsymbol{r}}$) and velocity ($\tilde{\boldsymbol{v}}$) vectors of the kite, and the S_K-components of the Earth's magnetic field ($\tilde{\boldsymbol{B}}$), the absolute angular velocity of the kite ($\tilde{\boldsymbol{\omega}}$), and the specific force ($\tilde{\boldsymbol{f}}$).

The Pitot tube of the PixHawk2™ , used in the precursor work,[20] was substituted by an Aeroprobe™ , micro Air Data System V2.0, which is composed of an onboard computer (see insets in Figure 2) and a multi-hole Pitot tube located at the tip of a boom. This sensor provides high-precision measurements of the kite true airspeed (TAS), angle of attack (AoA), and the angle of sideslip (AoS). These variables are denoted by $\tilde{v}_a$, $\tilde{\alpha}$, and $\tilde{\beta}$, respectively. A calibration at Mach = 0.03 performed by the system manufacturer guarantees the specifications of Table 1. The experiments for the LEI and RFD kites shown in this work were carried out with two different Pitot tubes, and they were used just after calibration. As compared with wind vanes, multi-hole Pitot tubes provide better measurements of $\tilde{\alpha}$ and $\tilde{\beta}$ at low airspeed, as well as a better dynamic response. Such a characteristic is crucial for the flight testing of kites because airflow speed can be below 5 m/s. Since the kites fly at high AoA (see Sections 3 and 4), the booms were mounted with an offset angle of 30° with respect to the x_K-axis in order to avoid the saturation of the instrument. This offset mounting is used for both kites and is highlighted in the top panel of Figure 2. The offset has been taken into account when we computed the true AoA of the kites, which is measured with respect to the x_K-axis. According to the range of the instrument (see Table 1), the experimental setup can capture AoA values from 10° to 50° and the instrument is saturated otherwise.

Having a rigid union between the boom supporting the Pitot tube and the kite is mandatory to guarantee the integrity of the air data measurements. Ideally, the boom and the kite should move as a rigid body. For the RFD kite, the boom was directly attached with a 3D printed interface to the kite central spine, which is a rigid carbon fiber tube with a diameter of 10 mm. In the case of the LEI kite, a 3D printed rig with the exact same shape of the central strut was designed and manufactured to attach the boom to the kite. This rig was secured to the strut by means of two adjustable straps. In addition, the boom was attached to the leading edge of the kite by using textile adhesive ribbons.

Additionally, the experimental setup was improved with a new wind station installed on the ground. The wind station has a rotatory platform that is orientated to the wind by means of a vane. A reference frame (S_V) with origin at the axis of rotation of the vane, x_V-axis pointing to the wind, and the z_V-axis parallel to the z_{NED}-axis, is introduced (Figure 1). The S_V-component of the Earth magnetic field ($\tilde{\boldsymbol{B}}_V$), the angular velocity of the vane with respect to S_E ($\boldsymbol{\omega}_V = \tilde{r}_V \boldsymbol{k}_V$), and the wind speed ($\tilde{\mathbf{V}}_w$) are measured by a PixHawk2™ hardware equipped with a Pitot tube. The experimental setup is completed with load cells that provide the tensions in all lines of the kites. Our model neglects tether inertia and assumes that the

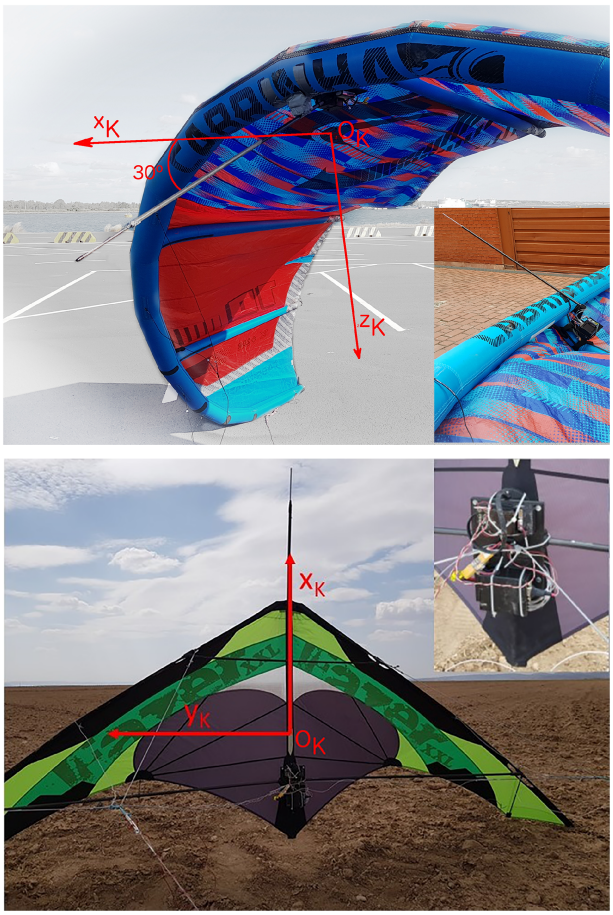

FIGURE 2 LEI (top) and RFD kites (bottom). The inset shows a detail of the the onboard instruments [Colour figure can be viewed at wileyonlinelibrary.com]

TABLE 1 Data sheet of the Aeroprobe™ micro Air Data System (sea level)

	Min. calibrated reading	Max. calibrated reading	Min. resolution	accuracy
TAS	2.5 ms^{-1}	20 ms^{-1}	0.11 ms^{-1}	±0.5 ms^{-1}
AoA	−20°	20°	0.1°	±1°
AoS	−20°	20°	0.1°	±1°

tensile forces measured by the sensors coincide with the tensions at the kite attachment points ($\tilde{T}_{A^{\pm}}$ and $\tilde{T}_{B^{\pm}}$). The observation vectors of the LEI and RFD kites then read

$$\tilde{\boldsymbol{y}}_{LEI} = \left[\tilde{\boldsymbol{r}}\ \tilde{\boldsymbol{v}}\ \tilde{\boldsymbol{f}}\ \tilde{\boldsymbol{\omega}}\ \tilde{\boldsymbol{B}}\ \tilde{v}_a\ \tilde{\alpha}\ \tilde{\beta}\ \tilde{T}_{A^+}\ \tilde{T}_{A^-}\ \tilde{T}_{B^+}\ \tilde{T}_{B^-}\ \tilde{\boldsymbol{B}}_V\ \tilde{r}_V\ \tilde{V}_w\ \tilde{D}\ \tilde{P}_{y_k}\right], \tag{1}$$

$$\tilde{\boldsymbol{y}}_{RFD} = \left[\tilde{\boldsymbol{r}}\ \tilde{\boldsymbol{v}}\ \tilde{\boldsymbol{f}}\ \tilde{\boldsymbol{\omega}}\ \tilde{\boldsymbol{B}}\ \tilde{v}_a\ \tilde{\alpha}\ \tilde{\beta}\ \tilde{T}_{A^+}\ \tilde{T}_{A^-}\ \tilde{\boldsymbol{B}}_V\ \tilde{r}_V\ \tilde{V}_w\ \tilde{D}\right], \tag{2}$$

In the observation vectors given by Equations (1) and (2), we added two constant variables that introduce information about the constraints. The first variable $\tilde{D}$ is the constant distance between O_E and O_K. After ignoring the small distance between the tether attachment points, the GPS antenna, and the center of mass of the kite, as well as tether elasticity effects, this distance is imposed by the tether length constraint. The second kinematic constraint only affects the LEI kite. We assumed that the projection $\tilde{P}_{y_K} = \overline{O_E O_A} \cdot \boldsymbol{j}_K$ vanishes, where $\overline{O_E O_A}$ is a vector with origin at O_E and tip at the middle of the segment delimited by A^+ and A^-.

Control of the kite is achieved by manual operation through a control bar. The design of this control bar is a novelty from the previous experimental setup, and it now houses the two loads cells in the lines of the RFD kite, and two of the four load cells in the lines of the LEI kite. The data of all the sensors were synchronized with a common triggering signal. The main characteristics of the kites, like mass, moments and products of inertia, surface, span, coordinates of the attachment points, and length of the front (L_l) and rear (L_t) lines, are shown in Table 2. Since the airspeed

TABLE 2 Characteristics of the LEI and RFD kites

	Cabrinha Switchblade	HQ Fazer XXL
m_K	3.4 kg	2 kg
I_x	8.68 kg m^2	0.72 kg m^2
I_y	2.43 kg m^2	0.09 kg m^2
I_z	8.40 kg m^2	0.81 kg m^2
I_{xz}	0.33 kg m^2	0 kg m^2
Surface	10 m^2	1.86 m^2
Span	4.3 m	3.6 m
$X_{A^{\pm}}$	0.42 m	0 m
$Y_{A^{\pm}}$	±1.05 m	±0.67 m
$Z_{A^{\pm}}$	−0.20 m	0 m
$X_{B^{\pm}}$	−0.97 m	–
$Y_{B^{\pm}}$	±2.15 m	–
$Z_{B^{\pm}}$	1.38 m	–
L_l	23.85 m	39.28 m
L_t	23.19 m	–

was in the order of 10 m/s, and the characteristic dimension of the kites is around 1 m, the Reynolds number was around 5×10^5. The aspect ratio of the LEI and the RFD kites are $AR \approx 1.84$ and $AR \approx 7$, respectively.

2.2 | FPR algorithm

The FPR algorithm is a continuous-discrete extended Kalman filter that has been adapted to include the special characteristics of the setup, like the tether constraints. The aerodynamic force and moment about O_K are part of the state vector and modelled as Gauss-Markov stochastic processes.[25,29,30] The continuous part of the filter is given by the process equation

$$\frac{d\boldsymbol{x}(t)}{dt} = \boldsymbol{f}_{proc}[\boldsymbol{x}(t)] + \bar{\boldsymbol{G}}\boldsymbol{w}(t). \tag{3}$$

A detailed description of the state vector ($\boldsymbol{x}$), the flow ($\mathbf{f}_{\text{proc}}$), and the process noise ($\boldsymbol{w}$), which is modeled as a multi-variable normal distribution function with zero mean and covariance $\bar{\boldsymbol{Q}}$, is in a previous work.[20] However, since the experimental setup was improved, some concepts need to be revisited and explained. The state vector of the filter has three different types of variables that we organize as

$$\boldsymbol{x} = [\boldsymbol{x}_k \;\; \boldsymbol{x}_{bias} \;\; \chi_1 \;\; \chi_2 \;\; \chi_3]. \tag{4}$$

Vector $\boldsymbol{x}_k = [\boldsymbol{r} \;\; \boldsymbol{v} \;\; \boldsymbol{\omega} \;\; \phi \;\; \theta \;\; \psi]$ is the kite state. It contains the S_E-components of the position vector of the kite's center of mass ($\boldsymbol{r} = \overline{O_E O_K} = x_E \boldsymbol{i}_E + y_E \boldsymbol{j}_E + z_E \boldsymbol{k}_E$), the S_K-components of the kite's velocity vector ($\boldsymbol{v} = d\boldsymbol{r}/dt = u\boldsymbol{i}_K + v\boldsymbol{j}_K + w\boldsymbol{k}_K$) and its angular velocity ($\boldsymbol{\omega} = p\boldsymbol{i}_K + q\boldsymbol{j}_K + r\boldsymbol{k}_K$), and the roll ($\phi$), pitch ($\theta$), and yaw ($\psi$) angles of the kite. The bias vector, $\boldsymbol{x}_{bias} = \left[\boldsymbol{\Theta}_{B_k} \; \boldsymbol{\Theta}_{B_V} \; \boldsymbol{\Theta}_{f_k} \; \boldsymbol{\Theta}_{\omega_k} \; \Theta_{V_w} \; \Theta_{r_V}\right]$, includes the biases of the error models for on-board measurements of the Earth's magnetic field ($\boldsymbol{\Theta}_{B_k}$), specific forces ($\boldsymbol{\Theta}_{f_k}$) and angular velocity ($\boldsymbol{\Theta}_{\omega_k}$), and the biases of the error models of the wind velocity (Θ_{V_w}), the angular velocity of the vane (Θ_{r_V}), and the magnetic field ($\boldsymbol{\Theta}_{B_V}$) measured by the sensors of the wind station. As shown in Equation (4), our state vector also includes the three *pseudo states vectors*

$$\boldsymbol{\chi}_i^{LEI} = [\boldsymbol{F}_{ai} \;\; \boldsymbol{M}_{ai} \;\; T_{A^+i} \;\; T_{A^-i} \;\; T_{B^+i} \;\; T_{B^-i} \;\; V_{wi} \;\; \psi_{wi}], \tag{5}$$

$$\boldsymbol{\chi}_i^{RFD} = [\boldsymbol{F}_{ai} \;\; \boldsymbol{M}_{ai} T_{A^+i} \;\; T_{A^-i} \;\; V_{wi} \;\; \psi_{wi}], \tag{6}$$

with $i = 1,2,3$. These vectors are governed by third-order Markov Models.[25,29,30] The first of these vectors, $\boldsymbol{\chi}_1$, contains the S_K-components of the aerodynamic force and moment about O_K ($\boldsymbol{F}_{a1}$ and $\boldsymbol{M}_{a1}$), the magnitudes of the tether tensions at the attachment points $T_{A\pm1}$ (and $T_{B\pm1}$ in the case

of the LEI kite), and the magnitude of the wind velocity V_{w1} and its heading angle ψ_{w1}. The process equations of vectors $\boldsymbol{\chi}_i$ with $i = 1,2,3$ yield a three-term quadratic interpolation as a function of time, whose coefficients are updated by the filter at each sampling instant (see Equation A3).

The measurement model, which is the discrete part of the filter, is

$$\tilde{\boldsymbol{y}} = \boldsymbol{h}(\boldsymbol{x}) + \boldsymbol{\eta}, \tag{7}$$

where $\tilde{\boldsymbol{y}}$ is the observation vector given by Equations (1) or (2), $\mathbf{h}(\mathbf{x})$ is the observation model that maps the true state space into the observed space, and $\boldsymbol{\eta}$ is the observation noise which is assumed to be a zero mean Gaussian white noise with covariance matrix $\bar{\boldsymbol{R}}$.

The detailed explanation of the application of the continuous-discrete EKF to Equations (3) and (7) and the input data provided by the sensors of the experimental setup is in a previous work.[20] Its application to our flight data for both kites, which exhibited robustness to the initialization of the filter, gives the time history of the state vector $\boldsymbol{x}(t)$. At every time step, the aerodynamic variables, that is, true airspeed (V_a or TAS), AoA (α), and AoS (β), were found from the state vector. For convenience, the aerodynamic force is projected in the wind reference frame S_w. Such a right-handed reference frame has origin at O_K, x_w-axis along the aerodynamic velocity vector, and the z_w-axis normal to the x_w-axis and contained in the plane of symmetry of the kite. The aerodynamic force and moment about O_K are

$$\boldsymbol{F}_a = -\frac{1}{2}\rho S V_a^2 [C_D \boldsymbol{i}_w - C_Y \boldsymbol{j}_w + C_L \boldsymbol{k}_w], \tag{8}$$

$$\boldsymbol{M}_a = \frac{1}{2}\rho S V_a^2 c [C_l \boldsymbol{i}_K + C_m \boldsymbol{j}_K + C_n \boldsymbol{k}_K], \tag{9}$$

where ρ is the air density, S and c are the surface and chord of the kite, and the brackets contain the aerodynamic coefficients of the kite.

3 | EXPERIMENTAL RESULTS FOR THE LEI KITE

The quantity and quality of the flight data obtained with the LEI kite are low because difficulties arose to fly the kite in cross-wind conditions and with high airspeed and tether tensions. These difficulties are intrinsic to our low cost experimental setup, which involves relatively short tether lengths and, due to limitations related to the load cells and the manual control system of the kite, it should operate with low wind speeds. Other experimental setups do not exhibit these issues and low AoA (around 10°) were measured by performing figure-eight trajectories in cross-wind conditions with a LEI kite.[22] Since the pilot could not perform figure-eight maneuvers, our kite flew in post-stall conditions most of the time and, around 1 min after takeoff, the kite crashed and the multi-hole Pitot tube was damaged. This lesson learned triggered the experimental activities with the RFD kite that, as shown in Section 4, were carried out successfully and with a new Pitot tube. However, some interesting records about the aerodynamics of the LEI kite were obtained before the accident and deserve attention.

Panel A of Figure 3 shows the projection of the trajectory in the $x_{NED} - y_{NED}$ plane where, for convenience, the horizontal and vertical axes correspond to the crosswind and downwind directions. The takeoff happened at the left side of the wind window and the kite flew from one side to the other several times until it crashed at the right side of the window. As shown in panels B and C, the tensions at the front lines were low (below 200 N) and the AoA measured by the Pitot tube was saturated most of the time. Such experimental evidence demonstrates that the AoA of the LEI kite was higher than 50° (see Section 2.1). However, during the pass that lasted from time 38.5 to 40.3 s, the velocity of the kite was

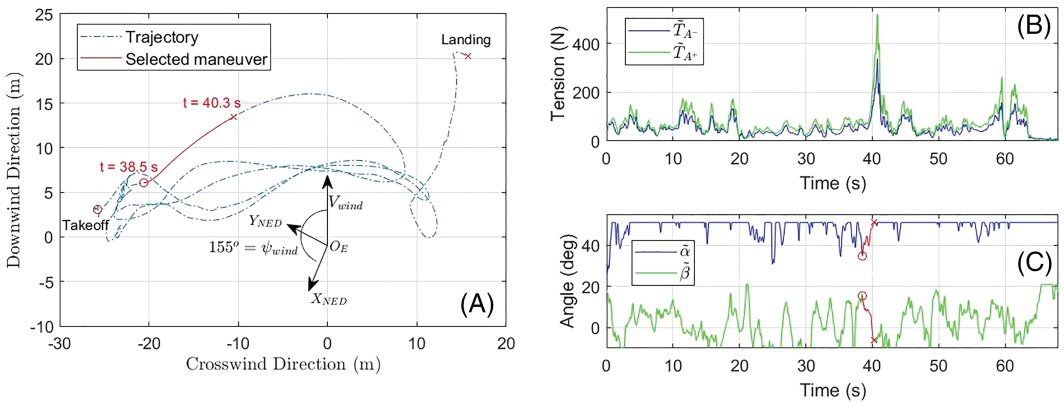

FIGURE 3 Trajectory of the LEI kite (A), tension at the front lines (B), and AoA measured by the Pitot tube (C) [Colour figure can be viewed at wileyonlinelibrary.com]

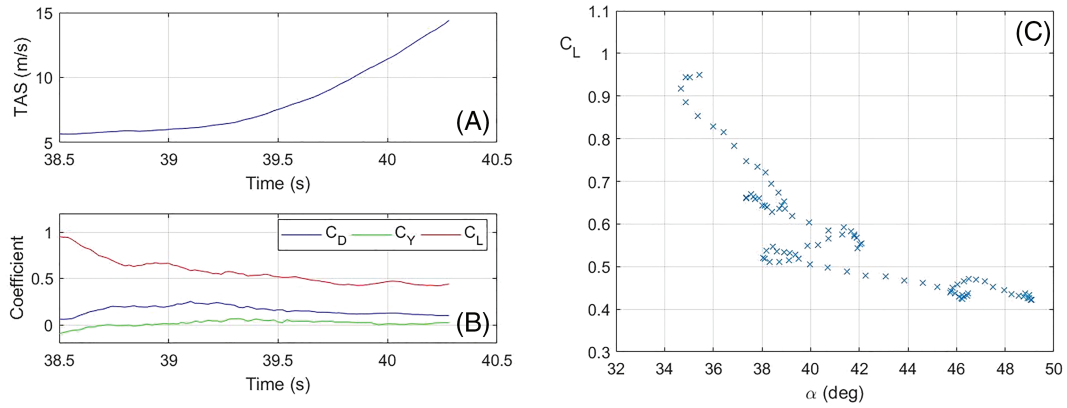

FIGURE 4 Time evolution of the TAS (A) and the aerodyamic coefficients (B) of the LEI kite. Lift coefficient versus angles AoA (C) [Colour figure can be viewed at wileyonlinelibrary.com]

large enough to produce a high tether tension (above 500 N). The Pitot tube measured an AoA that varied from 35° to 50° and the AoS decreased from 15° to −6°. The data obtained by the sensors during this interesting maneuver, which is highlighted with red color in panels A and C, were used to feed the FPR algorithm and get an estimation of the full state vector of the kite.

At the beginning of the selected maneuver, the kite is at a quasi-stationary state in the left corner of the wind window and has a positive roll angle of 50°. The weight of the kite and the tensions of the lines are mainly counter balanced by the lift and, to a lesser extent, by a (negative) aerodynamic lateral force. After the pilot pulled the right control line, the kite moved towards the zenit, while increasing its airspeed and altitude. The roll angle and the AoS decreased and became negative. Figure 4 displays quantitative results provided by the FPR algorithm during the maneuver. As shown in panel A, the TAS increased monotonically and reached a maximum of around 15 m/s. This feature explains the strong peak exhibited by the tensions of the front lines of panel B in Figure 3. The lift coefficient decreased from around 1 to below 0.5 because the kite was in post-stall conditions (see panel B). The AoA at the beginning of the maneuver was 35°, and it increased up to 50°, when the sensor was saturated. Such a feature is highlighted in panel C, which shows the value of C_L versus α provided by the FPR algorithm and exhibits the typical post-stall behavior. Unlike the lift coefficient, the variation of the drag coefficient was moderate. Its value at the beginning of the maneuver was around 0.06, reached a maximum of 0.25, and went down to 0.1. Regarding the lateral force coefficient, its behavior is consistent with the low AoS measured by the sensor. Initially, C_Y was negative, as expected for the positive AoS measured by the Pitot tube, and then it changed its sign when the AoS varied from 15° to −6°. Its absolute value remained small during the full maneuver.

4 | EXPERIMENTAL RESULTS FOR THE RFD KITE

Since its maneuverability was excellent, abundant flight data were obtained for the RFD kite. Panel A of Figure 5 shows the projection of the kite trajectory in the horizontal plane (blue dashed line). After the takeoff, which happened in the downwind direction, kite pitch angle equal to 90°, and aided by an assistant who propelled the kite upwards, more than 10 figure-eight trajectories were performed in the interval 20 s < t < 125 s.

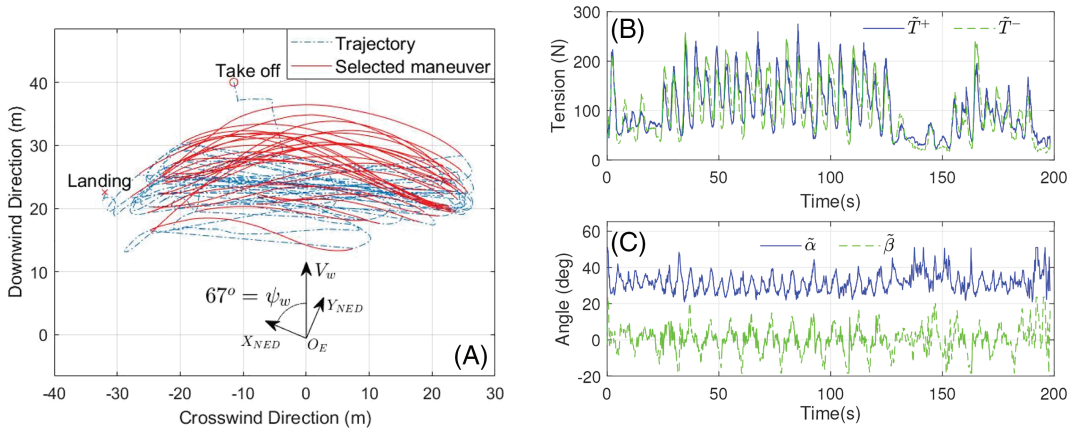

FIGURE 5 Trajectory of the RFD kite (A), tension at the front lines (B), and AoA and AoS measured by the Pitot tube (C) [Colour figure can be viewed at wileyonlinelibrary.com]

From t = 125 s to t = 150 s, the kite was steered to an equilibrium state close to the zenit and then a few more figure-eight trajectories of less amplitude were performed before the landing. In order to protect the Pitot tube, the kite was steered to the left side of the wind window slowly and an assistant grabbed it before touching the ground. Panel B shows the evolution of the tether tensions measured by the load cells. They exhibit a high repeatability and match very well with the expected behavior. For instance, the tensions in every figure-eight maneuver has two maxima and, depending on the travelling directions of the kite (left or right), the maxima of $\tilde{T}_{A+}$ is higher or lower than the one of $\tilde{T}_{A-}$. As expected, the measured tension was higher when the kite flew in cross-wind condition, and lower at the equilibrium state. The AoA and AoS varied within the ranges $20^\circ < \tilde{\alpha} < 50^\circ$ and $-18^\circ < \tilde{\beta} < 18^\circ$. Hereafter, we discuss the aerodynamics characteristics of the RFD kite in the selected maneuver, which is highlighted with a red solid line panel A of Figure 5 and corresponds with the figure-eight orbits in the interval $20\,\text{s} < t < 125\,\text{s}$. When these trajectories are examined in the crosswind direction versus altitude plane (not shown), straight and turning segments are identified.

Panels A and B in Figure 6 show the evolution during four figure-eight selected maneuvers of the TAS and the AoA measured by the sensors and estimated by the FPR algorithm, respectively. The estimated TAS and AoA are in good agreement with the air data computer raw measurements. From t = 34 s to t = 35 s, the TAS measurement was saturated, but the filter is still capable of reconstructing the kite aerodynamic speed, thus showing the robustness of the FPR algorithm. On the other hand, panels C–F display the aerodynamic coefficients provided by the FPR algorithm. The solid lines correspond to the selected straight segments, while the dashed lines correspond to the turns. The maxima (minima) of the TAS, which are reached during the straight (turning) segments, coincide in time with the maxima (minima) of the tether tensions in the panel B of Figure 5. When the TAS exhibits a maximum (minimum), the lift and the drag coefficients have a minimum (maximum) because the AoA decreases as the TAS increases in the straight segments. The time histories of these variables are smooth and have a high repeatability. The pitch moment coefficient (C_m) is small and negative for most of the flight. The lateral force coefficient (C_Y) is also small and, as expected due to the time history of the AoS, it changes its sign periodically.

For the straight segments of the figure-eight maneuvers, there are abundant data and, as the tensions are high, they are also expected to be the most reliable information to identify the aerodynamic parameters of the kite. For this particular set of data, a statistical analysis of the lift, drag, and pitch moment coefficients was carried out by using box plots. In these diagrams, the horizontal and central line of the box represents the median and the bottom and top edges indicate the 25th and 75th percentiles. The outliers are denoted with crosses and two vertical lines indicate the remaining data outside the central box that are not outliers. Data were gathered by AoA (intervals of width equal to 1°), and we made three different groups for the AoS: $|\beta| < 3$, $3 < |\beta| < 6$, and $6 < |\beta| < 9$. Panels A–C show the lift coefficient versus the angle of attack for these three groups of AoS. The fitting of the medians to a straight line gives the slops $C_{L\alpha} = 2.83, 2.42$ and 2.38 for $|\beta| < 3$, $3 < |\beta| < 6$, and $6 < |\beta| < 9$, respectively. These values are below the typical value for low-speed attached-flow lift-curve slope that, for $AR = 7$, is around 4 (see Figure 5 in Luckring[31]). The analysis of the drag coefficient (see panels D–F), besides showing the expected growth of C_D with C_L, highlights the important drag produced by the kite. For instance, for $C_L = 1$, one has $C_D \approx 0.4$ and the induced drag predicted by the lifting-line theory is only around $C_L^2/\pi ARe \approx 0.057$ for $AR = 7$ and a planform efficiency factor of $e = 0.8$. We finally mention that a similar analysis was carried out to study the behavior of the pitch moment coefficient (C_m) when the angle of attack is varied (not shown). The slope of the curve was around $C_{m\alpha} \approx -0.05$. A direct application of this identification of the aerodynamic parameters is the improvement of the aerodynamic model in two-line kite flight simulators.[32]

There are some interesting features in Figures 6 and 7 that require complementary analysis using computational fluid dynamics techniques. Even during the straight segments of the figure-eight maneuver, the kite does not fly in steady conditions because, beside wind fluctuations, the angular velocity does not vanish. This fact can explain the dispersion observed in some data of Figures 6 and 7. Moreover, previous comments about $C_{L\alpha}$ and C_D, and the high AoA measured during the flight, indicate that linear aerodynamic theories do not hold. For instance, the C_L versus α diagrams show that C_L grows monotonically even after reaching a high AoA. This may be due to nonlinear aerodynamic effects. It is well known that the typical angle of attack for maximum lift of a delta wing with low aspect ratio can be much higher (around 40°) than for a two-dimensional

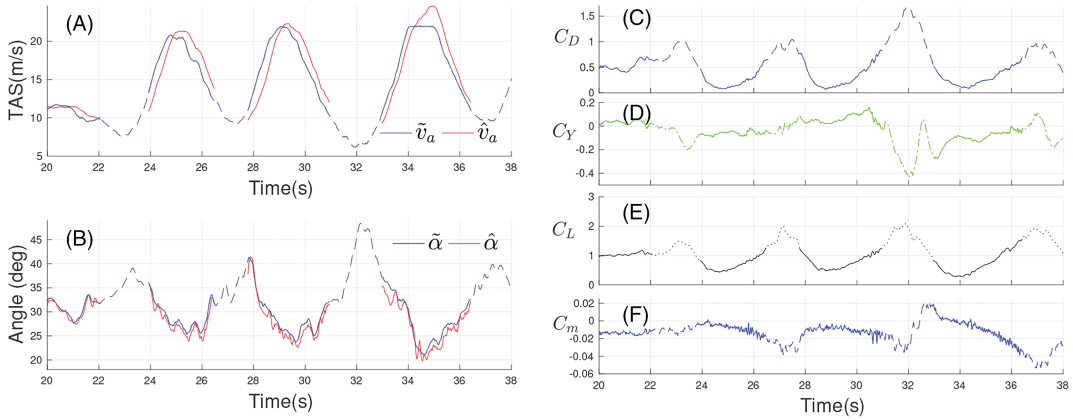

FIGURE 6 Evolution of the TAS, estimated AoA and the aerodynamics coefficients of the RFD kite during the figure-eight maneuvers [Colour figure can be viewed at wileyonlinelibrary.com]

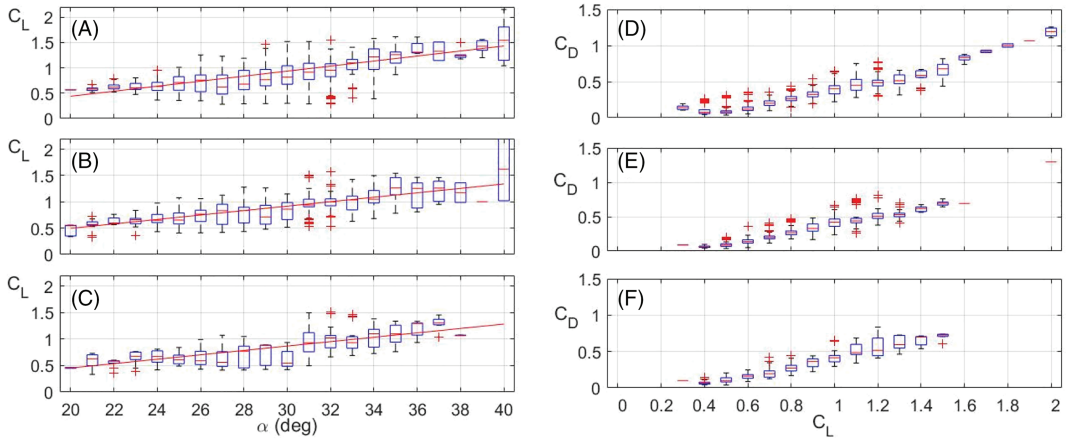

FIGURE 7 Lift coefficient versus angle of attack (panels A–C) and drag coefficient versus lift coefficient (panels D–F). The AoS was filtered within the ranges $|\beta| < 3$ (panels A and D), $3 < |\beta| < 6$ (panels B and E), and $6 < |\beta| < 9$ (panels C and F) [Colour figure can be viewed at wileyonlinelibrary.com]

airfoil due to the presence of two vortices.[33] The convex curvature of the flow near the leading edge produces a suction that increases the C_L. However, although panels A–C show a positive $C_{L\alpha}$ even at AoA around 40°, the results for low aspect ratio wings cannot be directly applied to our kite because it has $AR = 7$. Unsteady aerodynamic effects, like dynamic stall, can also increase the C_L and delay conventional flow separation on wings beyond the static stall angle.

5 | CONCLUSIONS

The estimation before modeling technique, which involves the combination of experimental data with a flight path reconstruction algorithm based on an extended Kalman filter, was shown to be a powerful tool to investigate the aerodynamic characteristics of LEI and RFD kites. Quantitative information about aerodynamic forces and moments as a function of the full state of the kites was obtained. This flight test method, which may be complementary to wind tunnel tests and computational fluid dynamic studies, could potentially play an important role in the design, modeling and optimization of airborne wind energy systems because the kites are tested in their true operational environment. Unlike previous works, the experimental setup included a high-precision multi-hole Pitot tube installed on a boom attached to the kites for direct measurements of the airspeed, angle of attack and sideslip angle of the kites. Despite its cost and vulnerability, and although the same information can be estimated from the wind velocity and the kite ground velocity, the multi-hole Pitot tube provides direct measurements of the flow that greatly improve the accuracy of the EKF algorithm. Adding the multi-hole Pitot tube, the wind station and the new configuration of the control bar increases the complexity of the experimental setup but, as shown by the data presented in this work, these sensors provide essential information for the aerodynamic study of the kites.

The results demonstrate that the LEI kite flew most of the time with an angle of attack above 50° in post-stall conditions. This statement, which cannot be extended in general to big AWE machines with long tethers, was corroborated and studied in detail for a particular maneuver that exhibited high airspeed and tether tensions. As expected for post-stall conditions, the lift coefficient decreased from 1 to 0.4 as the angle of attack increased from 35° to 50°. These conditions increase the risk of the experiment because of the associated low tether tensions and poor controllability of the kite. Indeed one of our Pitot tubes was broken because the kite crashed. This lesson learned suggests a reconfiguration of the experimental setup for large LEI kites in order to perform maneuvers with larger airspeeds and lower angles of attack. A transition from a manual to a mechanical control system, and from short to long tethers, is needed.

The behavior of the RFD kite was radically different. Although the AoA was high, between 20° and 40°, the slope of the C_L versus α curves provided by the filter was positive in the full AoA range. This resulted in a high tether tension and good controllability of the kite and allowed to obtain abundant data during more than 10 figure-eight maneuvers and perform a statistical analysis of the information of the filter. Aerodynamic parameters related with the lift, the drag, and the pitch moment coefficient were identified. Basic aerodynamic theories, like lifting-line theory, cannot explain the results. Although the aspect ratio of the kite is 7, the generation of strong vorticity in the leading edge of the kite and their unsteady dynamics may explain the high value of the AoA for maximum C_L observed in the experiments.

ACKNOWLEDGEMENTS

This work was initially supported by the Ministerio de Ciencia e Innovación of Spain and the European Regional Development Fund under the project GreenKite (ENE2015-69937-R, MINECO/FEDER, UE) and continued under the project GreenKite-2 (PID2019-110146RB-I00

/AEI/10.13039/501100011033) funded by the Agencia Estatal de Investigación of Spain. G. Sanchez-Arriaga's work is supported by the Ministerio de Economía, Industria y Competitividad of Spain under grant RYC-2014-15357. The authors thank C. Cobos for his assistance on the manufacturing of the sensor interfaces.

PEER REVIEW

The peer review history for this article is available at https://publons.com/publon/10.1002/we.2591.

ORCID

R. Borobia-Moreno https://orcid.org/0000-0003-4435-5113
R. Schmehl https://orcid.org/0000-0002-4112-841X
G. Sánchez-Arriaga https://orcid.org/0000-0002-8122-4051

REFERENCES

1. Ellington CP. The novel aerodynamics of insect flight: applications to micro-air vehicles. *J Exp Biol*. 1999;202(23):3439-3448.
2. Shyy W, Aono H, Chimakurthi SK, et al. Recent progress in flapping wing aerodynamics and aeroelasticity. *Prog Aerosp Sci*. 2010;46(7):284-327. https://doi.org/10.1016/j.paerosci.2010.01.001
3. Corke TC, Thomas FO. Dynamic stall in pitching airfoils: aerodynamic damping and compressibility effects. *Annu Rev Fluid Mech*. 2015;47(1):479-505. https://doi.org/10.1146/annurev-fluid-010814-013632
4. Choudhry A, Leknys R, Arjomandi M, Kelso R. An insight into the dynamic stall lift characteristics. *Exp Therm Fluid Sci*. 2014;58:188-208. https://doi.org/10.1016/j.expthermflusci.2014.07.006
5. Cherubini A, Papini A, Vertechy R, Fontana M. Airborne wind energy systems: a review of the technologies. *Renew Sust Energ Rev*. 2015;51(Supplement C):1461-1476. https://doi.org/10.1016/j.rser.2015.07.053
6. Lellis MD, Mendonça AK, Saraiva R, Trofino A, Lezana A. Electric power generation in wind farms with pumping kites: an economical analysis. *Renew Energy*. 2016;86:163-172. https://doi.org/10.1016/j.renene.2015.08.002
7. Paulig X, Bungart M, Specht B. Conceptual design of textile kites considering overall system performance. *Airborne wind energy*; 2013:547-562. https://doi.org/10.1007/978-3-642-39965-7_32
8. Fechner U, Vlugt R, Schreuder E, Schmehl R. Dynamic model of a pumping kite power system. *Renew Energy*. 2015;83:705-716. https://doi.org/10.1016/j.renene.2015.04.028
9. Sánchez-Arriaga G, Pastor-Rodríguez A, Sanjurjo-Rivo M, Schmehl R. A Lagrangian flight simulator for airborne wind energy systems. *Appl Math Modell*. 2019;69:665-684. https://doi.org/10.1016/j.apm.2018.12.016
10. Kheiri M, Nasrabad VS, Bourgault F. A new perspective on the aerodynamic performance and power limit of crosswind kite systems. *J Wind Eng Ind Aerodyn*. 2019;190:190-199. https://doi.org/10.1016/j.jweia.2019.04.010
11. Candade AA, Ranneberg M, Schmehl R. Structural analysis and optimization of a tethered swept wing for airborne wind energy generation. *Wind Energy*. 2020;23:1006-1025. https://doi.org/10.1002/we.2469
12. Mahdavi Nejad A, Tryggvason G. Power generation using kites in a GroundGen airborne wind energy system: a numerical study. *J Energy Resour Technol*. 2020;142:061306. https://doi.org/10.1115/1.4045700
13. Breukels J. An engineering methodology for kite design. *Ph.D. Thesis*; 2011. http://resolver.tudelft.nl/uuid:cdece38a-1f13-47cc-b277-ed64fdda7cdf
14. Leloup R, Roncin K, Bles G, Leroux J-B, Jochum C, Parlier Y. Estimation of the lift-to-drag ratio using the lifting line method: application to a leading edge inflatable kite. *Airborne wind energy*; 2013:339-355. https://doi.org/10.1007/978-3-642-39965-7_19
15. Bosch A, Schmehl R, Tiso P, Rixen D. Dynamic nonlinear aeroelastic model of a kite for power generation. *J Guid Control Dyn*. 2014;37(5):1426-1436. https://doi.org/10.2514/1.G000545
16. Thedens P, De Oliveira Andrade G, Schmehl R. Ram-air kite airfoil and reinforcements optimization for airborne wind energy applications. *Wind Energy*. 2019;22:653-665. https://doi.org/10.1002/we.2313
17. Folkersma M, Schmehl R, Viré A. Boundary layer transition modeling on leading edge inflatable kite airfoils. *Wind Energy*. 2019;22(7):908-921. https://doi.org/10.1002/we.2329
18. Viré A, Demkowicz P, Folkersma M, Roullier A, Schmehl R. Reynolds-averaged Navier–Stokes simulations of the flow past a leading edge inflatable wing for airborne wind energy applications. *J Phys Conf Ser*. 2020;1618:032007. https://doi.org/10.1088/1742-6596/1618/3/032007
19. Scupi A, Avital EJ, Dinu D, Williams JJR, Munjiza A. Large eddy simulation of flows around a kite used as an auxiliary propulsion system. *J Fluids Eng*. 2015;137(10):101301. https://doi.org/10.1115/1.4030482
20. Borobia R, Sanchez-Arriaga G, Serino A, Schmehl R. Flight-path reconstruction and flight test of four-line power kites. *J Guid Control Dyn*. 2018;41(12):2604-2614. https://doi.org/10.2514/1.G003581
21. Hummel J, Göhlich D, Schmehl R. Automatic measurement and characterization of the dynamic properties of tethered membrane wings. *Wind Energy Sci*. 2019;4(1):41-55. https://doi.org/10.5194/wes-4-41-2019
22. Oehler J, Schmehl R. Aerodynamic characterization of a soft kite by in situ flow measurement. *Wind Energy Sci*. 2019;4(1):1-21. https://doi.org/10.5194/wes-4-1-2019
23. Schmidt E, De Lellis Costa de Oliveira M, Saraiva R, Fagiano L, Trofino A. In-flight estimation of the aerodynamics of tethered wings for airborne wind energy. *IEEE Trans Control Syst Technol*. 2019;PP:1-14. https://doi.org/10.1109/TCST.2019.2907663
24. Ramachandran S, Schneider H, Mason J, Stalford H. Identification of aircraft aerodynamic characteristics at high angles of attack and sideslip using the estimation before modeling /EBM/ technique. In: Proceedings of the guidance, navigation, and control and co-located conferences American Institute of Aeronautics and Astronautics; 1977; Hollywood, FL, USA. https://doi.org/10.2514/6.1977-1169
25. Hoff JC, Cook MV. Aircraft parameter identification using an estimation-before-modelling technique. *Aeronaut J (1968)*. 1960;100(997):259-268. https://doi.org/10.1017/S000192400002889X

26. Hesse H, Polzin M, Wood TA, Smith RS. Visual motion tracking and sensor fusion for kite power systems. *Airborne wind energy: Advances in technology development and research*; 2018:413-438. https://doi.org/10.1007/978-981-10-1947-0-17
27. Fagiano L, Huynh K, Bamieh B, Khammash M. On sensor fusion for airborne wind energy systems. *IEEE Trans Control Syst Technol*. 2012;22:930-943. https://doi.org/10.1109/TCST.2013.2269865
28. Oehler J. Measuring apparent flow vector on a flexible wing kite. *MSc Thesis*; 2017. https://doi.org/10.18419/opus-9890
29. Sri-Jayantha M, Stengel RF. Determination of nonlinear aerodynamic coefficients using the estimation-before-modeling method. *J Aircr*. 1988;25(9):796-804. https://doi.org/10.2514/3.45662
30. Goszczyński JA, Michalski WJJ, Pietrucha JA. Estimation before modelling as the method for identification of the aircraft aerodynamic characteristics in nonlinear flight regime. *J Theor Appl Mech*. 2000;38(1):107–120. http://www.ptmts.org.pl/jtam/index.php/jtam/article/view/v38n1p107
31. Luckring JM. The discovery and prediction of vortex flow aerodynamics. *Aeronaut J*. 2019;123(1264):729-804. https://doi.org/10.1017/aer.2019.43
32. Sánchez-Arriaga G, García-Villalba M, Schmehl R. Modeling and dynamics of a two-line kite. *Appl Math Model*. 2017;47:473-486. https://doi.org/10.1016/j.apm.2017.03.030
33. Lee M, Ho C-M. Vortex dynamics of delta wings. *Frontiers in experimental fluid mechanics*; 1989:365-427. https://doi.org/10.1007/978-3-642-83831-6_8

How to cite this article: Borobia-Moreno R, Ramiro-Rebollo D, Schmehl R, Sánchez-Arriaga G. Identification of kite aerodynamic characteristics using the estimation before modeling technique. *Wind Energy*. 2021;1–13. https://doi.org/10.1002/we.2591

APPENDIX A: FLIGHT PATH RECONSTRUCTION ALGORITHM

This appendix provides details about the observation and the process models of the FPR algorithm. In particular, it gives the explicit form of vectors $\boldsymbol{f}_{proc}$ and $\boldsymbol{h}(x)$ in Equations (3) and (7), and the covariance matrices $\bar{\boldsymbol{Q}}$ and $\bar{\boldsymbol{R}}$. Only the elements of the FPR algorithm that are novel with respect to the one presented in Borobia et al.[20] are discussed.

Process Model

A comparison of Equation (4) with the state vector of Borobia et al.[20] reveals that the new variables of the filter are the biases of the sensors of the wind station that are governed by

$$\frac{d\Theta_{B_V}}{dt} = 0, \tag{A1}$$

$$\frac{d\Theta_{r_V}}{dt} = -\frac{\Theta_{r_V}}{\tau_{r_V}} + w_{r_V} \qquad \boldsymbol{w}_{r_V} \in N(0, \sigma^2_{w_{r_V}}), \tag{A2}$$

where τ_{r_V} is a constant and $\sigma^2_{w_{r_V}}$ is the variance of the driving noise w_{r_V}. For convenience, we recall that each of the three Markov vectors in Equation (5) has 12 components and we can denote them as χ_{ij} with $i = 1,...,3$ and $j = 1,...,12$. The process equations are then written in the compact form

$$\frac{d}{dt}\begin{pmatrix}\chi_{1j}\\ \chi_{2j}\\ \chi_{3j}\end{pmatrix} = \begin{pmatrix}0 & \gamma_{1j} & 0\\ 0 & 0 & \gamma_{2j}\\ 0 & 0 & 0\end{pmatrix}\begin{pmatrix}\chi_{1j}\\ \chi_{2j}\\ \chi_{3j}\end{pmatrix} + \begin{pmatrix}\xi_{1j}\\ \xi_{2j}\\ \xi_{3j}\end{pmatrix}, \tag{A3}$$

with γ_{1j} and γ_{2j} some constants, and ξ_{ij} taken from normal distribution functions with zero mean and variances $\sigma^2_{\xi_{F_A}}$, $\sigma^2_{\xi_{M_A}}$, $\sigma^2_{\xi_T}$, $\sigma^2_{\xi_{V_w}}$, and $\sigma^2_{\xi_{w_w}}$ for $j = 1,2,3$, $j = 4,5,6$, $j = 7,8,9,10$, $j = 11$, and $j = 12$, respectively. Finally, the noise vector $\boldsymbol{w}$ and matrix $\bar{\boldsymbol{G}}$ are

$$\boldsymbol{w} = \left[\boldsymbol{w}_f \;\; \boldsymbol{w}_\omega \;\; w_{V_w} \;\; w_{r_V} \;\; \xi_{1,1}\cdots \;\; \xi_{1,12}, \;\; \xi_{2,1}\cdots \;\; \xi_{2,12}, \;\; \xi_{3,1}\cdots \;\; \xi_{3,12}\right]^T, \tag{A4}$$

$$\bar{\boldsymbol{G}} = \begin{bmatrix}\bar{\boldsymbol{0}}_{18\times 44}\\ \bar{\boldsymbol{I}}_{44\times 44}\end{bmatrix}_{62\times 44}, \tag{A5}$$

TABLE A1 Parameters of the FPR algorithm

LEI Kite				RFD Kite			
Symbol	**Value**	**Symbol**	**Value**	**Symbol**	**Value**	**Symbol**	**Value**
$\gamma_{1,1\ldots6}$	0.1	$\gamma_{2,1\ldots6}$	0.1	$\gamma_{1,1\ldots6}$	0.1	$\gamma_{2,1\ldots6}$	0.1
$\gamma_{1,7\ldots10}$	1	$\gamma_{2,7\ldots10}$	1	$\gamma_{1,7\ldots10}$	1	$\gamma_{2,7\ldots10}$	1
$\gamma_{1,11}$	0.1	$\gamma_{2,11}$	0.1	$\gamma_{1,11}$	0.1	$\gamma_{2,11}$	0.1
$\gamma_{1,12}$	$10\pi/180$	$\gamma_{2,12}$	$10\pi/180$	$\gamma_{1,12}$	$10\pi/180$	$\gamma_{2,12}$	$10\pi/180$
τ_a	100 s	τ_ω	100 s	τ_a	100 s	τ_ω	100 s
τ_{V_w}	100 s			τ_{V_w}	100 s		
σ_{w_f}	0.2 m/s^2	σ_{w_ω}	$0.5\pi/180$ rad/s	σ_{w_f}	0.05 m/s^2	σ_{w_ω}	$0.1\pi/180$ rad/s
$\sigma_{w_{V_w}}$	0.002 m/s	$\sigma_{w_{r_V}}$	$0.5\pi/180$ rad/s	$\sigma_{w_{V_w}}$	0.001 m/s	$\sigma_{w_{r_V}}$	$0.1\pi/180$ rad/s
$\sigma_{\xi_{Fa}}$	17.0 N	$\sigma_{\xi_{Ma}}$	15.0 Nm	$\sigma_{\xi_{Fa}}$	10.0 N	$\sigma_{\xi_{Ma}}$	15.0 Nm
σ_{ξ_T}	3.0 N	$\sigma_{\xi_{V_w}}$	0.005 m/s	σ_{ξ_T}	5.0 N	$\sigma_{\xi_{V_w}}$	0.02 m/s
$\sigma_{\xi_{\psi w}}$	$0.8\pi/180$ rad			$\sigma_{\xi_{\psi w}}$	$0.1\pi/180$ rad		
σ_{η_B}	0.1 G	σ_{η_r}	2.0 m	σ_{η_B}	0.2 G	σ_{η_r}	5.0 m
σ_{η_v}	0.5 m/s	σ_{η_f}	0.2 m/s^2	σ_{η_v}	2.0 m/s	σ_{η_f}	4.0 m/s^2
σ_{η_ω}	$4.4\pi/180$ rad/s	$\sigma_{\eta_{V_a}}$	0.5 m/s	σ_{η_ω}	$8.0\pi/180$ rad/s	$\sigma_{\eta_{V_a}}$	1.0 m/s
σ_{η_α}	$0.5\pi/180$ rad	σ_{η_β}	$0.5\pi/180$ rad	σ_{η_α}	$0.5\pi/180$ rad	σ_{η_β}	$0.5\pi/180$ rad
σ_{η_T}	10.0 N	$\sigma_{\eta_{B_w}}$	0.01 G	σ_{η_T}	10.0 N	$\sigma_{\eta_{B_w}}$	0.02 G
$\sigma_{\eta_{rw}}$	$8.0\pi/180$ rad/s	$\sigma_{\eta_{V_w}}$	0.5 m/s	$\sigma_{\eta_{rw}}$	$4.0\pi/180$ rad/s	$\sigma_{\eta_{V_w}}$	0.5 m/s
σ_{η_D}	0.001 m	$\sigma_{\eta_{P_{ik}}}$	0.4	σ_{η_D}	0.01 m		

with $\bar{\boldsymbol{0}}$ a matrix with zeros and $\bar{\boldsymbol{I}}$ the identity matrix. The covariance matrix $\bar{\boldsymbol{Q}}$ has zeros everywhere except at the diagonal that reads

$$diag(\bar{\mathbf{Q}}) = \left[\sigma_{w_f}^2 \;\; \sigma_{w_f}^2 \;\; \sigma_{w_f}^2 \;\; \sigma_{w_\omega}^2 \;\; \sigma_{w_\omega}^2 \;\; \sigma_{w_\omega}^2 \;\; \sigma_{w_{V_w}}^2 \;\; \sigma_{w_{r_w}}^2 \;\; \sigma_{\xi_{1,1}}^2 \ldots \sigma_{\xi_{1,12}}^2 \;\; \sigma_{\xi_{2,1}}^2 \ldots \sigma_{\xi_{2,12}}^2 \;\; \sigma_{\xi_{3,1}}^2 \ldots \sigma_{\xi_{3,12}}^2\right]. \tag{A6}$$

The same methodology applies for the RFD kite, except that T_{B^+i} and T_{B^-i} do not appear in the Markov vector (see Equation 6) and index j runs from 1 to 10 (instead of 12) in the equations above. Table A1 shows the values of the parameter of the filter used in this work.

Observation model

The variables that are new in the observation vector are the angles measured by the multi-hole Pitot tube ($\tilde{\alpha}$ and $\tilde{\beta}$), the variables measured by the sensors of the wind station ($\tilde{\boldsymbol{B}}_V$, $\tilde{r}_V$, $\tilde{V}_w$), and the constraint of the LEI kite ($\tilde{P}_{yk}$). The airspeed was included in the observation vector of Borobia et al.,[20] but the observation model is different because the new setup has the information of the wind velocity provided by the wind station.

After writing the airspeed as $v_a = u_a \boldsymbol{i}_K + v_a \boldsymbol{j}_K + w_a \boldsymbol{k}_K$, the observation model for the measurements of the Air Data System V2.0 is

$$\tilde{v}_a = |\boldsymbol{v}_a| + \eta_{V_a}, \quad \eta_{V_a} \in N(0, \sigma_{\eta_{V_a}}^2), \tag{A7}$$

$$\tilde{\alpha} = \arctan\left(\frac{w_a}{u_a}\right) + \eta_\alpha, \quad \eta_\alpha \in N\left(0, \sigma_{\eta_\alpha}^2\right), \tag{A8}$$

$$\tilde{\beta} = \arcsin\left(\frac{v_a}{|\boldsymbol{v}_a|}\right) + \eta_\beta, \quad \eta_\beta \in N\left(0, \sigma_{\eta_\beta}^2\right), \tag{A9}$$

where $\boldsymbol{v}_a$ is computed from the state vector of the filter as

$$\boldsymbol{v}_a = \boldsymbol{v} + \boldsymbol{\omega} \times \overline{O_K P} - V_{w1} \bar{\boldsymbol{R}}_{EK}^T \begin{pmatrix} \cos\psi_{w1} \\ \sin\psi_{w1} \\ 0 \end{pmatrix}, \tag{A10}$$

with $\overline{O_K P}$ the vector with origin at the center of mass of the kite and tip at the position of the Pitot tube. In Equation (A10), we also introduced the rotation matrix

$$\bar{\boldsymbol{R}}_{EK} = \begin{pmatrix} c\psi c\theta & c\psi s\theta s\phi - s\psi c\phi & c\psi s\theta c\phi + s\psi s\phi \\ s\psi c\theta & s\psi s\theta s\phi + c\psi c\phi & s\psi s\theta c\phi - c\psi s\phi \\ -s\theta & c\theta s\phi & c\theta c\phi \end{pmatrix}, \tag{A11}$$

which depends on the yaw, pitch, and roll angles that are part of the state vector. For brevity, the cosine and sine of an angle were denoted with the letters c and s.

The observation model for the magnetometer installed in the wind station is

$$\tilde{\boldsymbol{B}}_V = \bar{\boldsymbol{R}}_{EV}^T \boldsymbol{B}_0 + \boldsymbol{\Theta}_{B_V} + \boldsymbol{\eta}_{B_V}, \quad \boldsymbol{\eta}_{B_V} \in N\left(0, \sigma^2_{\eta_{B_V}}\right), \tag{A12}$$

with B_0 the value of the magnetic field in the test area, and we introduced the rotation matrix that related S_E and S_V

$$\bar{\boldsymbol{R}}_{EV} = \begin{pmatrix} \cos\psi_V & -\sin\psi_V & 0 \\ \sin\psi_V & \cos\psi_V & 0 \\ 0 & 0 & 1 \end{pmatrix} \tag{A13}$$

and $\psi_V = \psi_{w1} + \pi$. Regarding the angular velocity of the vane and the wind velocity, we write

$$\tilde{r}_V = \gamma_{\psi_{w1}} \psi_{w2} + \Theta_{r_V} + \eta_{r_V}, \quad \eta_{r_V}, \in N\left(0, \sigma^2_{\eta_{r_V}}\right), \tag{A14}$$

$$\tilde{V}_w = V_{w1} + \Theta_{V_w}, \quad \eta_{V_w}, \in N\left(0, \sigma^2_{\eta_{V_w}}\right). \tag{A15}$$

Finally, the observation model for the projection of vector $\overline{O_E O_K}$ along $\boldsymbol{j}_K$ ($\tilde{P}_{j_K}$) is

$$\tilde{P}_{j_K} = \boldsymbol{j}_K \cdot \bar{R}_{EK}^T \boldsymbol{r} + \eta_{P_{j_K}}, \quad \eta_{P_{j_K}}, \in N\left(0, \sigma^2_{\eta_{P_{j_K}}}\right). \tag{A16}$$

$\tilde{P}_{j_K}$ is constant ($\tilde{P}_{j_K} = 0$) due to the constraints introduced by the tethers ($\overline{O_E A^+}$, $\overline{O_E A^-}$ and $\overline{A^+ A^-}$ defines an isosceles triangle).

The observation noise for the FPR algorithm of the LEI kite is

$$\boldsymbol{\eta} = \left[\boldsymbol{\eta}_{\mathbf{r}}\ \boldsymbol{\eta}_{\mathbf{v}}\ \boldsymbol{\eta}_{\mathbf{f}}\ \boldsymbol{\eta}_{\omega}\ \eta_B\ \eta_{va}\ \eta_\alpha\ \eta_\beta\ \eta_{T_{A^+}}\ \eta_{T_{A^-}}\ \eta_{T_{B^+}}\ \eta_{T_{B^-}}\ \boldsymbol{\eta}_{B_V}\ \eta_{\dot{r}_V}\ \eta_{V_w}\ \eta_D\ \eta_{P_{j_K}}\right]^T, \tag{A17}$$

and the covariance matrix $\bar{\boldsymbol{R}}$ has zeros everywhere except at the diagonal

$$\begin{aligned} diag(\bar{\boldsymbol{R}}) = \Big[&\sigma^2_{\eta_r}\ \sigma^2_{\eta_r}\ \sigma^2_{\eta_r}\ \sigma^2_{\eta_v}\ \sigma^2_{\eta_v}\ \sigma^2_{\eta_v}\ \sigma^2_{\eta_f}\ \sigma^2_{\eta_f}\ \sigma^2_{\eta_f}\ \sigma^2_{\eta_\omega}\ \sigma^2_{\eta_\omega}\ \sigma^2_{\eta_\omega}\ \sigma^2_{\eta_B}\ \sigma^2_{\eta_B}\ \sigma^2_{\eta_B}\ \sigma^2_{\eta_{va}}\ \sigma^2_{\eta_\alpha}\ \sigma^2_{\eta_\beta}\ \sigma^2_{\eta_T}\ \sigma^2_{\eta_T}\ \sigma^2_{\eta_T}\ \sigma^2_{\eta_T} \\ &\sigma^2_{\eta_{B_V}}\ \sigma^2_{\eta_{B_V}}\ \sigma^2_{\eta_{B_V}}\ \sigma^2_{\eta_{r_V}}\ \sigma^2_{\eta_{V_w}}\ \sigma^2_{\eta_D}\ \sigma^2_{\eta_{P_{j_K}}}\Big]. \end{aligned} \tag{A18}$$

In the case of the RFD kite, the observation model is exactly the same, except that the tensions of the rear lines ($\tilde{T}_B^{\pm}$) and one of the constraints ($\tilde{P}_{j_K}$) are removed. Table A1 summarizes the parameter of the observation model used in this work.